Three-Dimensional Viscous Flow Simulations over the VLS Using Overset Grids

E. Basso
CTA/IAE/ASE-N
12228-904 São José dos Campos, SP. Brazil
basso@iae.cta.br

J. L. F. Azevedo
CTA/IAE/ASE-N
12228-904 São José dos Campos, SP. Brazil
azevedo@iae.cta.br

The present work is inserted into an effort to develop a Chimera flow simulation code capable of handling general launch vehicle configurations. The paper is primarily concerned with presenting results of laminar and turbulent viscous simulations of flows over the first Brazilian satellite launch vehicle, the VLS, during its first-stage flight. The finite difference method is applied to the governing equations written in conservation-law form for general body conforming curvilinear coordinates. The spatial discretization is accomplished with a central difference scheme in which artificial dissipation terms, based on a scalar, non-isotropic model, are added to the numerical scheme to maintain stability. The time march process is accomplished with a 5-stage, 2nd-order accurate, Runge-Kutta scheme. The results here included are indicative of the current status of the Chimera flow simulation capability under development by the authors. The results also highlight interesting features of the flow over the complete VLS and point out the importance of the inclusion of viscous effects for flow simulation over such complex vehicles.
***Keywords**: Viscous simulations, chimera grids, finite difference method, satellite launcher*

Introduction

In the present work, laminar and turbulent viscous simulations are performed with the objective of demonstrating the capability currently available at Instituto de Aeronáutica e Espaço (IAE) for the aerodynamic analysis of launch vehicle flows. In particular, the work is interested in presenting detailed aerodynamic results for flows over the first-stage flight configuration of the first Brazilian satellite launcher vehicle (VLS), as a means of demonstrating the application of the available capability to the actual vehicle currently being qualified. The basic motivation for this work is, therefore, to provide a continuation in the development effort that has been going on in the institution here represented, which aims at creating the simulation capability to handle truly complex aerospace configurations. There is a strong interest in performing simulations over the VLS first-stage flight configuration, since this is a fairly complex vehicle with several bodies in close proximity. Three-dimensional results for the complete configuration were already obtained with the Euler formulation using the previous version of the Chimera flow simulation code under consideration here. The results are described in detail in Basso, Antunes and Azevedo (2000), together with a historical perspective of the development of CFD tools for flow simulation over general launch vehicle configurations at IAE. The inviscid calculations were not able to obtain good correlation with experimental data over some regions of the vehicle, regardless of the level of mesh refinement. In fact, there was some evidence that viscous effects could dominate the flow in such regions. In particular, over the region in which there is close proximity between the VLS central body and its strap-on boosters, it was not possible to obtain good comparisons between computational and experimental results with the inviscid solutions.[1]

The flight configuration of the first stage of the VLS is composed by a central body and four strap-on boosters arranged symmetrically around this central body, as one can observe in Fig. 1. This is, therefore, a quite complex geometry to be discretized by a structured mesh. Hence, there has been an effort to develop tools based on the overset, multiblock grid technique, or Chimera (Wang and Yang, 1994; Wang, Bunning and Benek, 1995), in order to simulate flows over the complete VLS vehicle. This technique provides the capability to use structured meshes for the discretization of the calculation domain over truly complex configurations. Moreover, it allows adaptive grid refinement characteristics, which are similar to those, achieved with unstructured meshes. The governing equations are written in conservative form and are discretized by a finite difference method. Spatial discretization uses second-order accurate, central difference operators. The time marching method is based on a 5-stage, Runge-Kutta algorithm (Jameson, Schmidt and Turkel, 1981), which has second-order accuracy in time. The artificial dissipation terms added are based on the non-isotropic, Turkel and Vatsa (1994) model.

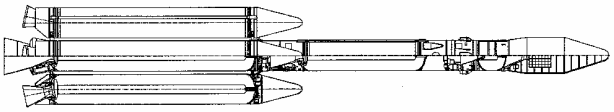

Figure 1. Schematic representation of the VLS system during its first-stage flight.

The implementation of viscous terms is carried out in the context of the Chimera code already available (Basso, Antunes and Azevedo, 2000) in order to perform the present studies. Moreover, since actual flight conditions over the VLS and similar vehicles consider Reynolds numbers, which typically are in the order of tens of millions, or higher, the Baldwin and Lomax (1978) model has been implemented and tested in the code. However, there are plans to extend the tests with this and other models in the future. Furthermore, in order to perform viscous flow simulations, it is necessary to generate grids, which are fine enough to provide support for capturing viscous effects throughout the flowfield. In the present case, since the afterbody portion of the vehicles is not included in the simulations, it is correct to state that viscous effects will be restricted to fairly thin boundary layers. Hence, for computational efficiency, grid refinement is particularly emphasized in the wall-normal direction and the simulations here presented should be considered as solutions of the thin- layer Navier-Stokes equations, despite the fact that more viscous terms are included in the equations actually implemented in the code.

The forthcoming sections present the governing equations together with details of the numerical method used for their solution. A brief discussion of the boundary conditions implemented is also presented, as well as an overview of the Chimera grid procedure used in the present code. Viscous laminar and turbulent solutions for the complete VLS vehicle are presented and discussed. Finally, a

Paper accepted November, 2004. Technical Editor: Aristeu da Silveira Neto.

critical evaluation of the flow simulation capability implemented at IAE is presented, followed by a discussion of perspectives for future work.

Nomenclature

Cp = pressure coefficient
d = artificial dissipation operator
$\bar{E}$ = flux vector in the ξ direction
e = total energy per unit of volume
$\bar{F}$ = flux vector in the η direction
$\bar{G}$ = flux vector in the ς direction
J = Jacobian of the transformation
L = characteristic length
M = Mach number
Pr = Prandtl number
$\bar{Q}$ = vector of conserved variables
Re = Reynolds number
RHS = right-hand-side operator
u = Cartesian velocity component in the x direction
v = Cartesian velocity component in the y direction
w = Cartesian velocity component in the z direction

Greek Symbols

α = angle of attack and constants of Runge-Kutta scheme
Δt = time step
τ = time
ξ = longitudinal direction in curvilinear coordinates
η = wall-normal direction in curvilinear coordinates
ς = azimuthal direction in curvilinear coordinates
ρ = air density
δ = standard 3-point central difference operator
$\bar{\delta}$ = standard mid-point central difference operator

Subscripts

∞ = relative to non-disturbed flow
i, j, k = relative to a generic point
v = relative to viscosity

Superscripts

l = relative to stage of Runge-Kutta scheme
n = iteration

Governing Equations

It is assumed that the flows of interest can be represented by the Reynolds-averaged Navier-Stokes equations in three dimensions. These equations can be written in conservation-law form for a curvilinear coordinate system as

$$\frac{\partial \bar{Q}}{\partial \tau} + \frac{\partial}{\partial \xi}\left(\bar{E} - \bar{E}_v\right) + \frac{\partial}{\partial \eta}\left(\bar{F} - \bar{F}_v\right) + \frac{\partial}{\partial \varsigma}\left(\bar{G} - \bar{G}_v\right) = 0 , \quad (1)$$

where $\bar{Q}$ is the vector of conserved variables, defined as

$$\bar{Q} = J^{-1}\left[\rho, \rho u, \rho v, \rho w, e\right]^T . \quad (2)$$

In these equations, ρ is the density, u, v and w are the Cartesian velocity components and e is the total energy per unit of volume. The $\bar{E}$, $\bar{F}$, and $\bar{G}$ are the inviscid flux vectors, and $\bar{E}_v$, $\bar{F}_v$, and $\bar{G}_v$ are the viscous flux vectors. The complete expressions for the inviscid flux vectors can be found in Vieira *et al*. (1998), and expressions for the viscous $\bar{Q}_v$ flux vectors, as implemented here, can be found, for instance, in Antunes (2000). It is important to emphasize that, consistent with previous comments, the cross derivative terms were eliminated in the definition of the viscous flux vectors. Expressions for the Jacobian of the transformation, J, as well as for the various metric terms can be found in Vieira *et al.* (2000) and in Pulliam and Steger (1980), among other references. The pressure can be obtained from the equation of state for a perfect gas. A suitable nondimensionalization of the governing equations has been assumed in order to write Eq. (1). In particular, the values of flow properties are made dimensionless with respect to freestream quantities, as described in Pulliam and Steger (1980).

The governing equations are discretized in a finite difference context on structured hexahedral meshes, which would conform to the bodies in the computational domain. Since a central difference spatial discretization method is being used, artificial dissipation terms must be added to the formulation in order to control nonlinear instabilities. The artificial dissipation terms used here are based on Turkel and Vatsa's scalar model (Turkel and Vatsa, 1994). This model is nonlinear and non-isotropic, with the scaling of the artificial dissipation operator in each coordinate direction weighted by its own spectral radius of the corresponding flux Jacobian matrix. The residue operator is defined as being the evaluation of the discretized partial differential equation, or system of partial differential equations, and, in this way, it represents how well the evaluation of the discretized form of the equations is being satisfied by the current solution, in the present iteration level *n*. The artificial dissipation terms are added to the residue operator to maintain nonlinear stability. In the present implementation, the residue operator is defined as

$$\begin{aligned} RHS^{(l)}_{i,j,k} = \Delta t_{i,j,k} \Big[& \delta_\xi \left(\bar{E}\right)_{i,j,k} - \bar{\delta}_\xi \left(\bar{E}_v + J^{-1} d\right)_{i,j,k} \\ & + \delta_\eta \left(\bar{F}\right)_{i,j,k} - \bar{\delta}_\eta \left(\bar{F}_v + J^{-1} d\right)_{i,j,k} \\ & + \delta_\varsigma \left(\bar{G}\right)_{i,j,k} - \bar{\delta}_\varsigma \left(\bar{G}_v + J^{-1} d\right)_{i,j,k} \Big] . \end{aligned} \quad (3)$$

Here, the δ_ξ, δ_η and δ_ς terms represent standard 3-point central difference operators in the ξ, η and ς directions, respectively. Similarly, $\bar{\delta}_\xi$, $\bar{\delta}_\eta$ and $\bar{\delta}_\varsigma$ are the mid-point central difference operators. The artificial dissipation operators, $d_{i\pm 1/2, j, k}$ $d_{i, j\pm 1/2, k}$ and $d_{i, j, k\pm 1/2}$, which appear from the application of the difference operators are defined precisely as described in Turkel and Vatsa's (1994) model.

The time march is performed based on a 5-stage, 2nd-order accurate, hybrid Runge-Kutta time-stepping scheme,

$$\begin{aligned} & Q^{(0)}_{i,j,k} = Q^{n}_{i,j,k} , \\ & Q^{(l)}_{i,j,k} = Q^{(0)}_{i,j,k} - \alpha_l \, RHS^{(l-1)}_{i,j,k} \quad , l = 1,...,5 , \\ & Q^{n+1}_{i,j,k} = Q^{(5)}_{i,j,k} . \end{aligned} \quad (4)$$

Here, the α_l constants are defined as α_1=1/4, α_2=1/6, α_3=3/8, α_4=1/2, α_5=1. It should be emphasized that only the convective operator inside the *RHS* term is actually evaluated at every time step. The viscous flux vectors are only evaluated at the first stage of the Runge-Kutta time-stepping scheme. Moreover, the artificial dissipation terms are evaluated at alternate stages, i.e., at the odd stages of the time-march procedure. It can be shown that this provides enough damping to maintain nonlinear stability (Jameson, Schmidt and Turkel, 1981; Swanson and Radespiel, 1991), whereas it yields a more efficient numerical scheme. Since steady state solutions are the major interest of the present study, a variable time step convergence acceleration procedure has been implemented. Further details on the variable time step procedure implemented can be found, for instance, in Basso, Antunes and Azevedo (2000) and in Antunes (2000).

Finally, turbulent flow simulations have used the Baldwin and Lomax (1978) algebraic eddy viscosity model, in its standard form, as described in the original paper by Baldwin and Lomax (1978). Since this model is well known and its expressions are widely available, its equations will not be included here.

Results and Discussion

Laminar Viscous Simulations

The first set of results discussed in the paper considers viscous simulations over the VLS without the inclusion of a turbulence closure model. However, the Reynolds numbers of interest for actual VLS flows are very high and the flow is undoubtedly turbulent over the vast majority of the vehicle surface. Therefore, despite the title used for this section, the authors are not concerned with simulations, which are truly "laminar", but with Navier-Stokes results without the inclusion of a turbulence model despite the high flow Reynolds numbers considered. Although under these conditions, the physical meaning of such flow simulation results is questionable, this approach has been followed due to two reasons. First and foremost, as the forthcoming discussion will show, such "laminar" viscous simulations already provide insight into important features of the flow over the complete VLS. Aside from this fact, this intermediate stage of the CFD code development should be seen as a necessary evolutionary step towards the complete flow simulation capability.

The meshes used for the first viscous simulations of the flow over the complete VLS had 120 x 36 x 33 points in the ξ, η and ς directions, respectively, for each of the booster grids and 120 x 65 x 33 points for the central body. This grid is referred here as the coarse grid. Throughout the present paper, ξ denotes the vehicle longitudinal direction, η is the wall-normal direction and ς is the azimuthal direction. Furthermore, the grids for the individual components of the configuration were generated independently through algebraic grid generation methods. These grids have exponential stretching from the wall, with spacing growth rate of 10%. The actual complete configuration is used in the simulations, namely, the central body and four boosters are included in the definition of the computational domain. In these simulations, the freestream Mach number is assumed to be M_∞ = 2.0 and the angle of attack is zero. The Prandtl number is set to Pr = 0.72, and the Reynolds number is 10 million, based on the diameter of the central body of the vehicle. In order to facilitate the presentation of flow simulation results, Fig. 2 shows a schematic frontal view of the vehicle and it defines flow planes in which results are discussed here.

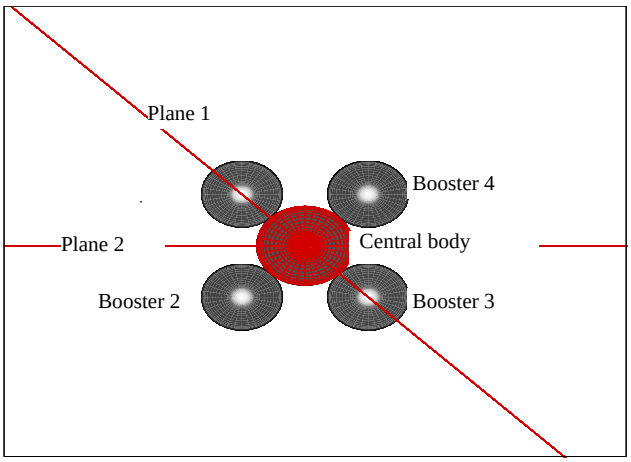

Figure 2. Top view of complete VLS configuration indicating some of the planes in which vehicle results are presented.

Figure 3 is a visualization of the Mach number contours in the longitudinal plane denominated "plane 1" in Fig. 2. The boundary layer thickening along the central body surface, in the region immediately upstream of the lateral boosters, can be clearly seen in Fig. 3. The thickening of the boundary layer is a result of the detached bow shock, ahead of the boosters, impingement on the central body surface. The information on the pressure rise due to shock impingement propagates upstream through the boundary layer and, eventually, causes flow separation upstream of the impingement point due to the weakening of the boundary layer momentum. Boundary layer separation, on the other hand, causes the creation of an oblique shock wave, which is not clearly seen in Fig. 3. This oblique shock wave is more readily seen on pressure

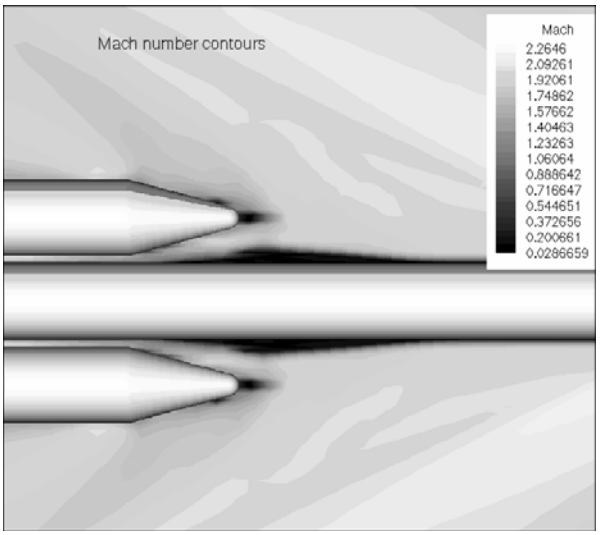

Figure 3. Mach number contours on plane 1 (Fig. 2) for laminar flow simulations with the coarse grid (M_∞ = 2, α = 0 deg., Re = 10 million).

contour plots. It is important to point out that these flow features ahead of the booster nose caps are not present in the Euler simulations reported in Basso, Antunes and Azevedo (2000). This indicates that, even with coarse grids, the viscous solutions are providing flow structures, which are different from the ones seen in the Euler cases.

Figure 4 presents the velocity vectors on a flow plane, which contains the central body axis and the axes of two boosters (plane 1 in Fig. 2). In particular, Fig. 4 is showing the details of the flowfield

just upstream of the booster forward aerodynamic fairing. It should be emphasized that only velocity vectors corresponding to grid points in the central body mesh, in the cited plane, are represented in this figure. Velocity vectors associated with points in the booster grid were suppressed from the figure in order to allow for a better visualization of the flowfield in the region. Flow deviation

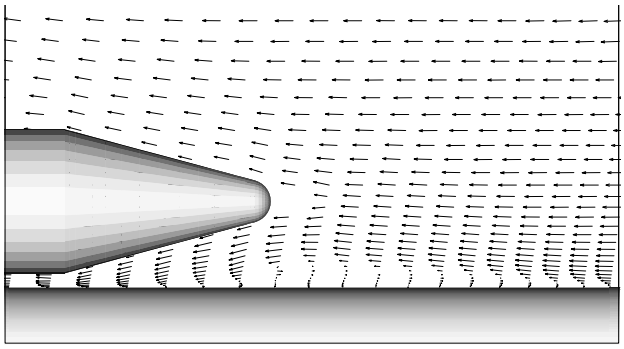

Figure 4. Detail of the velocity vector plot around the booster nose cap for laminar simulations with the coarse grid (M_∞ = 2, α = 0 deg., Re = 10 million).

due to the booster is clearly seen in this figure. Furthermore, one can also clearly see in the figure the recirculation region, which extends from approximately 2.5 booster diameters upstream of the booster nose until well within the conical booster section. The velocity profiles along a portion of this separation region seem also to indicate that there is even a secondary separation within the recirculation region. The streamline plot shown in Fig. 5 illustrates this last observation.

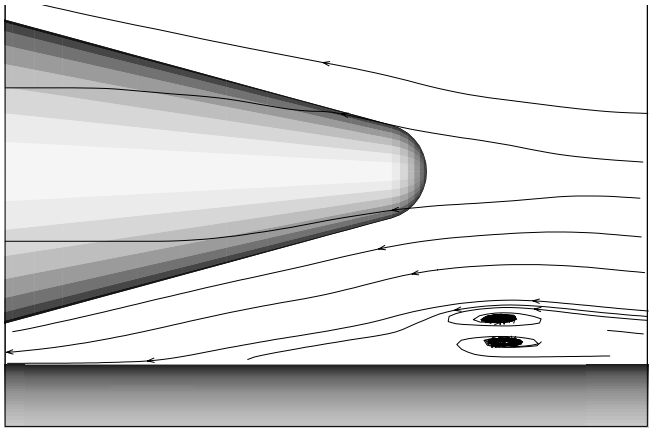

Figure 5. Streamlines near the booster nose for coarse grid laminar simulations (M_∞ = 2, α = 0 deg., Re = 10 million).

Pressure coefficient distributions on plane 1, along the vehicle central body wall, are shown in Fig. 6. It presents a comparison of the current Navier-Stokes results without turbulence modeling with experimental data, and with the pressure coefficient distribution obtained from the inviscid calculations reported in Basso, Antunes and Azevedo (2000) for a finer grid. One can observe that, in the forward portion of the vehicle, the agreement between computational and experimental data is quite good, except for discrepancies, which can be observed in the boattail region.

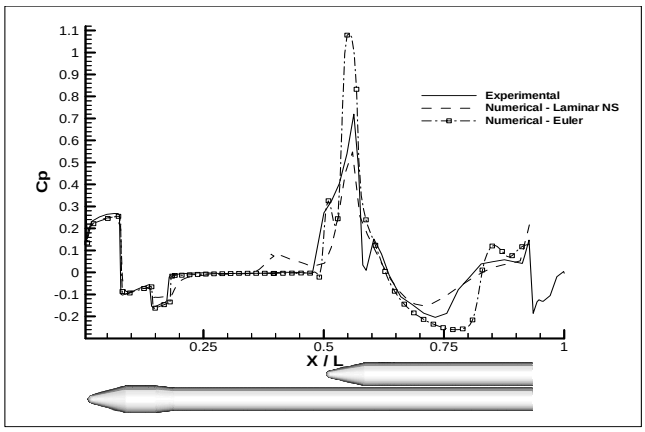

Figure 6. Pressure coefficient distributions for plane 1 along central body wall for coarse grid laminar simulations (M_∞ = 2, α = 0 deg., Re = 10 million).

Concerning the discrepancies observed in the boattail region, previous experience with axisymmetric calculations (Azevedo and Buonomo, 1999) has indicated that a very fine mesh is required to correctly capture the flow topology. Essentially, at supersonic freestream conditions, there is an oblique shock impinging on the boattail-afterbody cylinder intersection. This shock interacts with the body boundary layer, creating a region in which fairly complex flow phenomena are present and, hence, a very fine grid in the longitudinal direction is required for accurately capturing the flow physics. Such a fine grid in the boattail region was not used in the present case because the computational resources available would not allow for the needed refinement in this region, and there was an understanding that it would be more relevant, in the present case, to provide a better description of the region with strong interaction between central body and boosters. In any event, since the origin of the discrepancies observed in the boattail region are well understood and the emphasis here is in the flow near the boosters, the authors consider that further discussion of comparisons in the forward portion of the vehicle is beyond the scope of the present paper.

A sudden increase in the pressure coefficient distribution is observed at x/L $\cong$ 0.35 for the computational solution. The increase in Cp is due to the oblique shock wave created by the separation region along the central body. The experimental data does not have such pressure coefficient increase, clearly indicating that the experimental measurements do not see an oblique shock wave at this region in the flow. This could be explained by the fact that, at Re = 10 million, the flow is turbulent. A turbulent boundary layer does not separate as easily due to an adverse pressure gradient as a laminar boundary layer. Hence, the flow separation upstream of the booster nose, which eventually is the originator of the oblique shock, can be simply a result of the lack of turbulence modeling under conditions in which the flow is actually turbulent.

Further downstream, at x/L $\cong$ 0.50, the experimental measurements indicate a kink in the pressure coefficient distribution. This corresponds to the booster detached bow shock impingement on the central body. Clearly, the computational results do not display such effect due to the presence of the oblique shock wave upstream of the boosters. The position of the pressure peak at x/L $\cong$ 0.57 is correctly captured by the computation, although the magnitude of the pressure peak has a fairly significant error. There is a second pressure peak at x/L $\cong$ 0.61, which the computational results simply ignore. Downstream of this second pressure peak, there is a region with reasonably good agreement between experimental and computational data but, downstream of x/L $\cong$ 0.70, the discrepancies between computational and experimental results

again become significant. One should observe, however, that the computational mesh used in these simulations corresponds to the coarse grid used for the inviscid calculations reported in Basso, Antunes and Azevedo (2000). Hence, it is to be expected that mesh refinement should contribute to improvements in the correlation between computation and experiments.

A refined mesh was generated with 220 x 50 x 67 grid points for the central body mesh and 200 x 40 x 33 points for each of the booster meshes. As before, these numbers refer to grid points in the ξ, η and ς directions, respectively, and the individual grids have a 10% exponential grid stretching in the wall-normal direction. This grid is referred to here as the fine grid. Moreover, this grid only contains half of the central body and two boosters, yielding a total of approximately 1.3 million grid points, which is pretty much in the upper limit for the computational resources available to the authors at the time. This grid implies in a factor of four increases in the azimuthal direction resolution of the central body grid and almost a factor of two increases in the longitudinal resolution of both central body and booster grids. Furthermore, since these launchers only fly at very low angles of attack, the consideration that the flow is symmetric about the pitching plane is not a severe restriction in the usefulness of the computations for design work. The same flight condition was considered for the simulations with the fine grid. Therefore, $M_\infty = 2.0$, the angle of attack is zero, Pr = 0.72, and the Reynolds number is 10 million, based on the diameter of the central body of the vehicle.

Figure 7 presents pressure contours on plane 1 (see Fig. 2) obtained for the simulation with the fine grid. This figure only shows the flowfield around the nose cap of the boosters. In this case, the oblique shock wave upstream of the boosters, due to the flow separation previously described, is clearly evident in the figure. Moreover, the detached shock in front of the boosters and its interaction with the oblique shock are also clearly seen in the pressure contours. The rapid expansion, which occurs as the flow passes over the booster cone-cylinder intersection, is also evident in Fig. 7. Hence, it is clear that the flow in this interaction region around the nose of the boosters is quite complex.

Pressure coefficient distributions along the central body, and on plane 1 (see Fig. 2), are shown in Fig. 8. As before, this figure compares experimental and viscous computational results, and it also includes the inviscid results reported in Basso, Antunes and Azevedo (2000), for the corresponding grid. It is clear that mesh refinement has improved the correlation between the results along the boattail region in the forward portion of the vehicle.

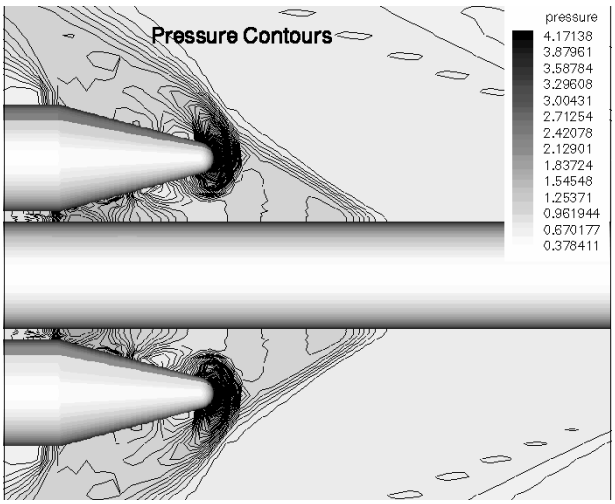

Figure 7. Dimensionless pressure contours along plane 1 for fine grid laminar simulations ($M_\infty = 2$, $\alpha = 0$ deg., Re = 10 million).

However, the agreement is still not perfect in this region. The oblique shock wave due to flow separation ahead of the boosters is even more pronounced in this case, with a much better defined and stronger pressure jump at $x/L \cong 0.42$. The position of the pressure peak at $x/L \cong 0.57$ is again adequately captured by the calculation but, as before, the magnitude of the peak is still smaller than the experimental value. The difference in Cp peak magnitude is, however, smaller in this case than it was for the coarse grid results.

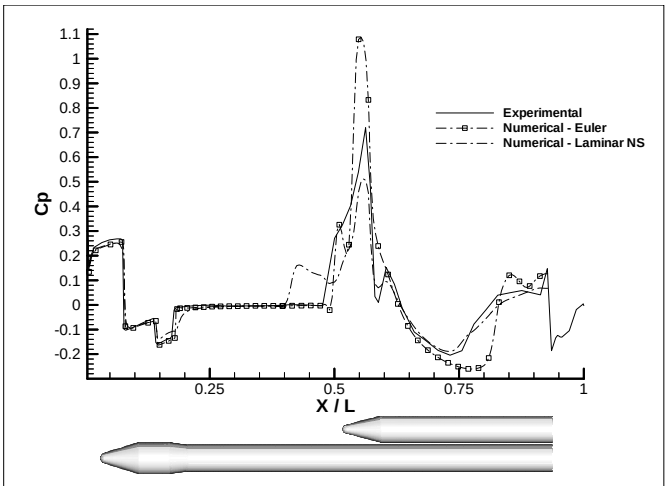

Figure 8. Pressure coefficient distributions for plane 1 along central body wall for fine grid laminar simulations ($M_\infty = 2$, $\alpha = 0$ deg., Re = 10 million).

Moreover, as one can clearly see in Fig. 8, the simulation starts to capture the second pressure peak at $x/L \cong 0.61$. Furthermore, the agreement between experimental and computational Cp distributions downstream of this second pressure peak is remarkably good throughout the remaining of the vehicle. It must be emphasized that the present computations do not represent the vehicle nozzle region and, hence, it is not possible to match the results downstream of the $x/L \cong 0.92$ station. A comparison of the Euler calculations discussed in Basso, Antunes and Azevedo (2000) and the results in Fig. 8 indicate that the flow in the downstream sections of the vehicle include important viscous effects. Therefore, there would be no way of obtaining good agreement between experiments and computation without the inclusion of viscous terms in the formulation.

Turbulent Viscous Simulations

For the flight conditions here considered which essentially involve VLS flows with Reynolds numbers in the order of 10^7 based on the body diameter, flowfields are clearly turbulent. Therefore, the implementation of turbulence models in the code is a necessary step in order to provide an adequate representation of the flow. The long-term objective of this work is to have a suite of models available in the code and let the user select the model that better suits his/her application. It is envisaged that, for the relevant flow conditions for the VLS, especially at angle of attack, a one-equation or a two-equation eddy viscosity model will be necessary for a correct representation of the flowfields. As an initial step towards this goal, a simple algebraic model has been implemented in the code, represented by the algebraic Baldwin and Lomax (1978) model in its standard form. This section describes results obtained with this model.

The mesh used for the turbulent computations has 220 x 50 x 35 points, in the ξ, η and ς directions, respectively, for the central body grid and 180 x 40 x 33 points for each booster grid. As in the previous case, the pitch plane is assumed to be a symmetry plane in the flowfield and, hence, only half of the central body and two boosters are represented in the computational domain. The flight condition considered for these simulations is identical to the one considered in the previous cases. Moreover, here the turbulent Prandtl number was set to 0.9, which is consistent with other results reported in the literature (Pulliam and Steger, 1980). For these flow conditions and mesh, values of y^+ for the first grid point off the wall in the range of 2 to 3 are obtained. Previous experience (Azevedo and Buonomo, 1999) indicates that such range of values of y^+ is completely adequate for simulations with the Baldwin and Lomax model.

Figure 9 presents the Mach number contours for this simulation in the plane containing the axes of the central body and two boosters (plane 1 in Fig. 2). An observation of Fig. 9 indicates that the flowfield solution in this case is not much different from that obtained for the laminar calculations with the fine grid. In particular, one can clearly see the flow separation ahead of the boosters, along the central body, and the oblique shock wave which is formed upstream of this separation region. Actually, the flow separation region seems to be even larger in this case and it clearly extends further upstream than in the laminar calculations. It must be emphasized that the implementation of the Baldwin and Lomax (1978) model has been validated in the work of Antunes (2000). Therefore, the model is being directly used in the present VLS simulations without any additional discussion regarding an assurance of its correct implementation.

Figure 10 presents a comparison of pressure coefficient distributions along the central body for plane 1 (see Fig. 2). The curves shown in this figure include the experimental data, the turbulent computational results and the computational results without turbulence modeling obtained with the fine mesh. It is evident from the figure that the separation occurs further upstream in the turbulent simulation when compared to the previous solution. Furthermore, the agreement between computation and experiment, in the region downstream of the second pressure peak ($x/L \cong 0.61$), is poorer for the turbulent simulations that it was for the calculations without turbulence modeling on the fine grid. The two grids are not identical, but they are sufficiently similar to rule out the possibility that the differences could be credited to the grid. Finally, Fig. 11 presents the flow streamlines in the region around the booster nose cap for the turbulent simulation, and it shows details of the separated flow in this region. It is clear that the computations are indicating a fairly complex separated region, certainly including secondary separation within the original reversed flow bubble. It is, therefore, quite questionable whether the Baldwin and Lomax model would be able to truly represent such a physically complex separated boundary layer, if the computational results were an accurate representation of the experimentally observed flowfield. The experimental pressure distributions, however, show no evidence of a separation region in this portion of the vehicle at this flight condition.

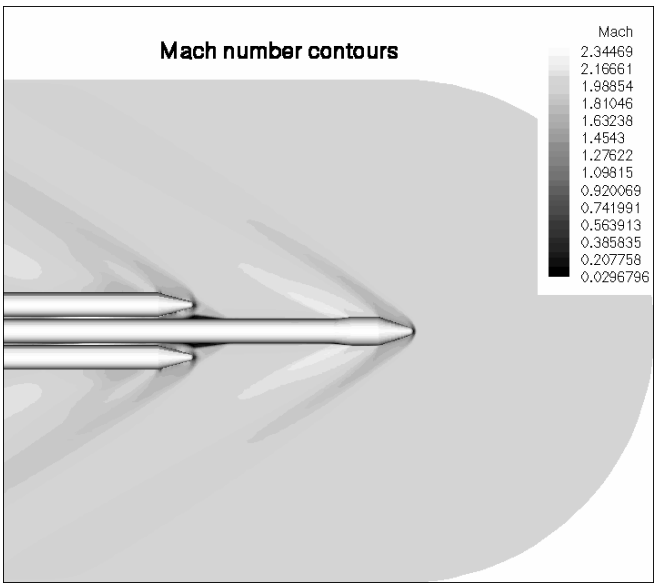

Figure 9. Mach number contours in the field (plane 1) for turbulent simulations ($M_\infty = 2$, $\alpha = 0$ deg., Re = 10 million).

The initial expectation was that the application of a turbulence model could improve the correlation between numerical and experimental data, in comparison with the type of agreement obtained in the previous section in which no turbulence modeling was employed. In particular, there was expectation that the separation region upstream of the boosters would disappear and, hence, so would the oblique shock wave, which is formed due to the separation. Clearly, this is not what the present results have shown. Furthermore, it is well known that the Baldwin and Lomax model has a tendency to add more eddy viscosity than what would actually be the correct amount to represent the correct physical behavior of the boundary layer. Hence, this means that the model has a tendency of stabilizing boundary layers that, actually, should separate. This compounds even further the questions with regard to the present turbulent simulations. On the other hand, the Baldwin and Lomax algebraic model has obtained having in mind fairly simple boundary layer flows. Therefore, it should come as no surprise the fact that this model was not able to improve the representation of the complex flowfield around the boosters of the complete VLS configuration. The present simulations, actually, serve the role of highlighting the importance of having more advanced turbulence closure models available for handling the complex flowfields over the VLS (Bigarella, Basso and Azevedo, 2004). As previously stated, the long term objective is to have advanced one-equation or two-equation eddy viscosity models available in the code, but this subject is beyond the scope of the present effort. Finally, one should also observe that at least one very important conclusion, concerning high speed flows over the VLS, can be drawn from the present results. The very good agreement obtained for the pressure distributions between the experiment and the fine grid "laminar" simulation, downstream of $x/L \cong 0.61$, is a very strong indicator that the flow in this region of very close proximity between central body and booster is dominated by viscous effects.

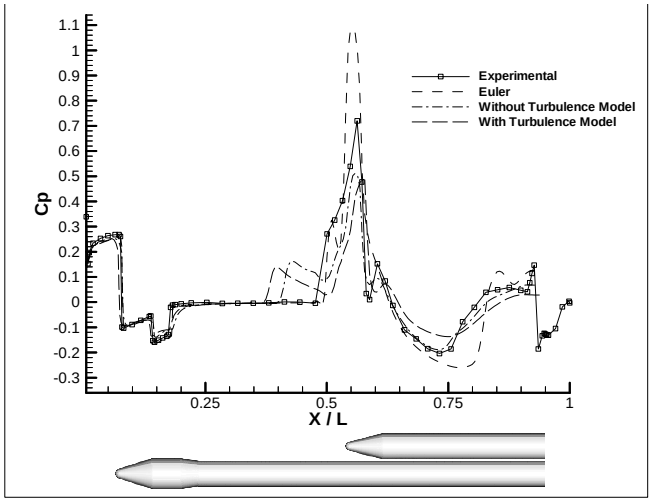

Figure 10. Comparison of pressure coefficient distributions along the central body wall for plane 1 (M_∞ = 2, α = 0 deg., Re = 10 million).

The fact that the comparison between experiment and computation becomes worse in this region with the inclusion of a simple turbulence model stresses this conclusion even further. In other words, the relevant mechanism that determines the flow in this region is associated with viscous effects and not with turbulent transport phenomena. Although the determination of the most relevant physical mechanism at play in the region of close proximity between the VLS central body and its boosters might seem to be a simple contribution, it must be said that it is a question that has concerned the CFD group at IAE for quite some time (see, for instance, Zdravistch and Azevedo, 1991).

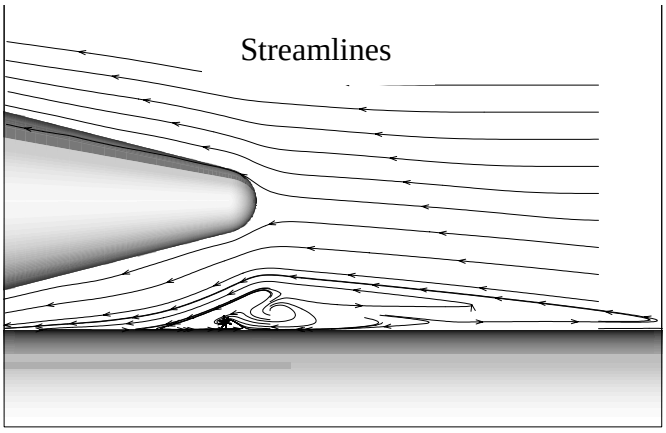

Figure 11. Detail of streamlines around the separation region for turbulent simulations (M_∞ = 2, α = 0 deg., Re = 10 million).

Concluding Remarks

The paper describes viscous computations over the complete VLS vehicle. These calculations use a Chimera grid approach together with a finite difference numerical method to simulate supersonic flows over the complete VLS configuration including the central body and the strap-on boosters. Spatial discretization uses a central difference scheme plus added artificial dissipation terms. These are formed as a blend of second and fourth differences with an appropriate pressure switch, which detects the present of strong pressure gradients. Temporal discretization uses an explicit, 5-stage, 2nd-order accurate Runge-Kutta time stepping scheme with a spatially variable time step option for convergence acceleration for steady state problems. Algebraic grids are generated for each body of the complete configuration and these are coupled together in a Chimera sense in order to generate the complete composite grid for the overall configuration.

Despite the fact that Reynolds numbers of interest are of the order of 10^7, numerical results without turbulence modeling are presented for two different meshes for the sake of code development and to provide a broader assessment of the various physical aspects which could effect the complex flowfield over the vehicle. The first mesh has approximately 830,000 grid points and it envelops the complete vehicle, whereas the other has approximately 1.3 million grid points and treats the pitch plane as a symmetry plane. Results for the fine grid calculations show very good qualitative agreement with the experimental data for pressure coefficient distributions, except for the appearance of an oblique shock upstream of the booster nose cap region due to flow separation of the central body boundary layer. In particular, the quantitative agreement between experiments and fine grid computational results for pressure coefficient distributions is very good in the downstream region of the flow. Such an agreement demonstrates the need to include the viscous terms in order to correctly capture the phenomena present in the region of strong aerodynamic interaction between central body and boosters. Finally, results for turbulent simulations using the Baldwin and Lomax algebraic eddy viscosity model are presented. These results indicate the need of more advanced turbulence closure models in order to adequately describe the complexity of the present flow.

Acknowledgments

The present work was partially supported by Conselho Nacional de Desenvolvimento Científico e Tecnológico, CNPq, under the Integrated Project Research Grant No. 501200/2003-7. The authors are also indebted to Núcleo de Atendimento em Computação de Alto Desempenho, NACAD-COPPE/UFRJ, and to Centro Nacional de Supercomputação, CESUP/UFRGS, which have provided the computational resources used for the present simulations.

References

Antunes, A.P., 2000, "Simulation of Aerodynamic Flows Using Overset Multiblock Meshes," Master Dissertation, Department of Aeronautical Engineering, Instituto Tecnológico de Aeronáutica, São José dos Campos, SP, Brazil, (in Portuguese, original title is "Simulação de Escoamentos Aerodinâmicos Utilizando Malhas de Blocos Múltiplos Sobrepostos").

Azevedo, J.L.F., and Buonomo, C.A., 1999, "Axisymmetric Turbulent Simulations of Launch Vehicle Forebody Flows," AIAA Paper No. 99-3528, 30th AIAA Fluid Dynamics Conference and Exhibit, Norfolk, VA.

Baldwin, B.S., and Lomax, H. L., 1978, "Thin Layer Approximation and Algebraic Model for Separated Turbulent Flows," AIAA Paper 78-257.

Basso, E., Antunes, A..P., and Azevedo, J.L.F., 2000, "Three Dimensional Flow Simulations Over a Complete Satellite Launcher With a Cluster Configuration," AIAA Paper No. 2000-4514, Proceedings of the 18th AIAA Applied Aerodynamics Conference, Vol. 2, Denver, CO, pp. 805-813.

Bigarella, E.D.V., Basso, E., and Azevedo, J.L.F., 2004, "Centered and Upwind Multigrid Turbulent Flow Simulations with Applications to Launch Vehicles," AIAA Paper No. 2004-5384, Proceedings of the 22nd AIAA Applied Aerodynamics Confernece and Exhibit, Providence, RI.

Jameson, A., Schmidt, W., and Turkel, E., 1981, "Numerical Solutions of the Euler Equations by Finite Volume Methods Using Runge-Kutta Time-Stepping Schemes," AIAA Paper No. 81-1259.

Pulliam, T.H., and Steger, J.L., 1980, "Implicit Finite-Difference Simulations of Three-Dimensional Compressible Flow," AIAA Journal, Vol. 18, No. 2, pp. 159-167.

Swanson, R.C., and Radespiel, R., 1991, "Cell Centered and Cell Vertex Multigrid Schemes for the Navier-Stokes Equations," AIAA Journal, Vol. 29, No. 5, pp. 697-703.

Turkel, E., and Vatsa, V.N., 1994, "Effect of Artificial Viscosity on Three-Dimensional Flow Solutions," AIAA Journal, Vol. 32, No. 1, pp. 39-45.

Vieira, R., Azevedo, J.L.F., Fico, N.G.C.R., Jr., and Basso, E., 1998, "Three Dimensional Flow Simulation in the Test Section of a Slotted Transonic Wind Tunnel," ICAS Paper No. 98-R.3.11, Proceeding of the 21st Congress of the International Council of the Aeronautical Sciences, Melbourne, Australia (publication in CD-ROM format without page numbering).

Wang, Z.J., Buning, P., and Benek, J., 1995, "Critical Evaluation of Conservative and Non-Conservative Interface Treatment for Chimera Grids," AIAA Paper No. 95-0077, 33rd AIAA Aerospace Sciences Meeting and Exhibit, Reno, NV.

Wang, Z.J., and Yang, H.Q., 1994, "A Unified Conservative Zonal Interface Treatment for Arbitrarily Patched and Overlapped Grids," AIAA Paper No. 94-0320, 32nd AIAA Aerospace Sciences Meeting and Exhibit, Reno, NV.

Zdravistch, F., and Azevedo, J.L.F., 1991, "Simulation of the Interference Region on a Multiblody Satellite Launcher," Proceedings of the 11th ABCM Mechanical Engineering Conference – COBEM 91, Blue Volume, São Paulo, SP, pp. 205-208.